


# Filament extrusion-based additive manufacturing of NiTi shape memory alloys

**Journal Article****Author(s):**

Wagner, Marius A.; Ocana-Pujol, Jose L.; Hadian, Amir; [Clemens, Frank Jörg](#) ; Spolenak, Ralph

**Publication date:**

2023-01

**Permanent link:**

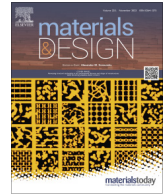
<https://doi.org/10.3929/ethz-b-000591871>

**Rights / license:**

[Creative Commons Attribution-NonCommercial-NoDerivatives 4.0 International](#)

**Originally published in:**

Materials & Design 225, <https://doi.org/10.1016/j.matdes.2022.111418>



# Filament extrusion-based additive manufacturing of NiTi shape memory alloys



Marius A. Wagner<sup>a,\*</sup>, Jose L. Ocana-Pujol<sup>a</sup>, Amir Hadian<sup>b</sup>, Frank Clemens<sup>b</sup>, Ralph Spolenak<sup>a,\*</sup>

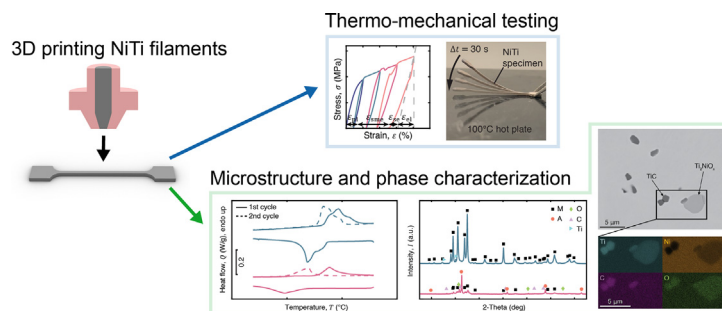
<sup>a</sup>Laboratory for Nanometallurgy, Department of Materials, ETH Zürich, 8093 Zürich, Switzerland

<sup>b</sup>Laboratory for High Performance Ceramics, Empa, 8600 Dübendorf, Switzerland

## HIGHLIGHTS

- Filament extrusion-based additive manufacturing of NiTi shape memory alloys with superelastic and shape memory properties.
- Characterization of thermo-mechanical properties and microstructure.
- Additive manufacturing of actuator geometries.

## GRAPHICAL ABSTRACT



## ARTICLE INFO

### Article history:

Received 5 September 2022

Revised 19 November 2022

Accepted 21 November 2022

Available online 26 November 2022

## ABSTRACT

Integrated additive manufacturing of actuators based on active materials could potentially replace conventional motors in numerous applications across disciplines like biomedical engineering, robotics, or aerospace. In this work, extrusion-based additive manufacturing of functional NiTi shape memory alloys is demonstrated via 3D printing of filaments consisting of thermoplastic binder and metal powder. Two alloys are fabricated, one showing superelastic, the other showing shape memory properties at room temperature. The microstructures of both alloys are characterized and set into perspective with the measured thermo-mechanical properties. The 3D-printed NiTi showed a shape memory strain of 1.9 %, respectively a superelastic strain of 1.3 % for an applied strain of 4 %. To enlarge the shape memory strain actuator geometries are designed, fabricated, and tested. The results of this study may find application in the field of additive manufacturing of active structures, also referred to as 4D printing. Commonly, polymeric materials are used in such structures, which often suffer from poor mechanical properties and durability. The use of metallic materials as it is investigated in this work could help to overcome these limitations.

© 2022 The Authors. Published by Elsevier Ltd. This is an open access article under the CC BY-NC-ND license (<http://creativecommons.org/licenses/by-nc-nd/4.0/>).

## 1. Introduction

Active materials, able to undergo changes in shape, offer a potential alternative to conventional motors for actuation and allow for integrated fabrication processes. Paired with the unprecedented design freedom of additive manufacturing (AM)

techniques, active materials bear large potential for the creation of structures or architected materials with unprecedented functionalities. In the research field of 4D printing, most studies use polymeric materials to create active structures or metamaterials by harnessing the shape changing capabilities of these materials. The low strength and actuation force, as well as the low fatigue resistance and susceptibility to ageing imposes large limitations on the state-of-the-art structures made from polymers [1]. This makes the transition from lab-scale proof of concepts to real world

\* Corresponding authors.

E-mail addresses: [marius.wagner@mat.ethz.ch](mailto:marius.wagner@mat.ethz.ch) (M.A. Wagner), [ralph.spolenak@mat.ethz.ch](mailto:ralph.spolenak@mat.ethz.ch) (R. Spolenak).

applications challenging. The employment of shape memory alloys (SMAs) for actuation has the potential to overcome many of the current limitations, as they stand out due to their exceptionally high actuation energy density (up to  $2 \text{ kJ kg}^{-1}$ ) [2] and they are more durable than many common polymeric active materials. This makes shape memory alloys a prime candidate for actuator applications in 3D-printed active structures.

Actuators based on SMAs exhibit low complexity, can be miniaturized, are reliable, and silent [3,4]. NiTi is to date the most widespread SMA, due to its excellent shape memory strain and actuation stress [5]. Hence, NiTi has found application in biomedical engineering [6], automotive, and aerospace industry [7]. The shape memory effect in NiTi is induced thermally by a reversible phase transformation from the martensite to the austenite phase.

The synergistic relationship between the shape memory properties of the SMAs and the complex geometries accessible through AM has been demonstrated by recent studies. Examples are 3D-printed Mg-NiTi composites with high damping and energy absorption capacity (NiTi scaffolds were 3D-printed, Mg was added by melt infiltration) [8], shape-changing structures [9], simple inch worm robots [10], or lattice structures [11–14]. Additionally, difficulties in conventional machining like tool wear can be circumvented by additive techniques, which is especially relevant for NiTi [15,16].

The vast majority of research on AM of SMAs is performed using powder bed fusion (PBF). Besides NiTi alloys [8–13,17–20], CoNiGa high temperature SMAs [21], CuAlNi [22,23], ferrous SMAs [24,25], and magnetic NiMnGa SMAs [26–28] have been fabricated by PBF. Directed energy deposition was used for fabrication of NiTi [29,30], CuAlNi [31], and CoNiGa [32]. In addition, NiTi has been fabricated via Wire arc AM [33,34]. Binder jetting was used for AM of NiMnGa [35–37] and solvent on granule jetting was demonstrated for NiTi [38]. Significantly less research has been performed in the field of material extrusion-based AM of SMAs. Ink writing was used for fabrication of NiTi SMAs [39,40] and NiMnGa magnetic SMAs [41]. To the authors' best knowledge, there exists only one publication using fused filament fabrication of metals (FFFm) to print SMAs using NiTi [42]. This work reported the feedstock compounding and filament preparation. Three sintering conditions were compared. Besides the NiTi phase, NiTi<sub>2</sub>, and Ni<sub>3</sub>Ti phases were observed, and microhardness measurements were performed. The study lacks an investigation of the phase transition temperatures and thermo-mechanical properties.

This work aims to extend the current state of research, providing a more in-depth study on NiTi 3D-printed via the filament extrusion-based AM technique FFFm. The focus of this study is twofold. On the one hand, the microstructure and resulting thermo-mechanical properties of the 3D-printed NiTi are studied. On the other, different actuator geometries are fabricated with the goal to increase the amount of actuation strain compared to the bulk material obtained.

The maximum shape memory strain of SMAs is fundamentally limited by the underlying phase transformations of the alloy. One strategy to overcome this limit is the design of actuator geometries which reduce the local strain in the material for a given applied global strain. This can be achieved by conversion of a global uniaxial deformation into local shear or bending through an engineered geometry. A simple example for this is a straight wire which is transformed into a spring. Coiled spring actuators exhibit a considerable increase in the range of motion compared to a straight wire. This however, comes at the price of lower actuation force, as the material is loaded in shear instead of tension [4,43]. Bending of beam geometries feature the same characteristics by converting uniaxial deformation into bending of thin beams or sheets [4,44]. In general, the maximum deformation, which can be recovered depends on the stress and strain induced in the thin members,

which should stay below the critical limit to induce slip. Comparable conversions in deformation mode can be achieved in cellular solids with bending dominated topologies. This was recently demonstrated for NiTi triply periodic minimal surface structures fabricated by SLM, which showed a shape memory strain of 4.8 % [13]. A second approach to convert large deformations into small local bending strain is by using a highly porous foams, which in fact are cellular solids with bending dominated topologies [45]. NiTi foams are widely researched for their good shape memory and superelasticity, tunable mechanical properties, and biocompatibility [46–50]. If the foam walls are sufficiently thin in relation to the cell size, the local strain in the walls can be reduced, similar to strain in the spring actuator discussed above.

One could also think of a combined approach in which a global uniaxial deformation is first converted into bending of a structural component, e.g. a bending beam, and the tensile and compressive strains in the beam are then converted into bending of the walls or struts of a highly porous microstructure. A similar hierarchical approach was recently demonstrated for NiTi hierarchical cellular structures, with different levels of porosity, fabricated by SLM [14]. The structures showed almost complete superelastic recovery when compressed to strains of 3 %. Yet, the potential of actuator designs utilizing such hierarchical architectures remains not fully explored.

This study aims to lay a foundation for FFFm of actuators and active mechanical metamaterials made from NiTi SMAs. The microstructures and thermo-mechanical properties of two alloys are investigated, one exhibiting superelasticity, the other exhibiting a shape memory effect at room temperature. Different actuator geometries are explored to increase the recoverable strain of the 3D-printed SMA.

## 2. Experimental procedure

### 2.1. Materials preparation

The filaments were prepared by mixing Ar-atomized pre-alloyed NiTi powder (NiTi-1, Ni content 50.5 at.%; NiTi-2, Ni content 50.1 at.; Eckart TLS GmbH, Germany) with binder polymers. The chemical composition and particle size distribution of the two powders according to measurements performed by the supplier are shown in Table 1. A SEM micrograph of the two powders can be found in the Supplementary Information, Fig. S1. The primary powders in this study were selected such that one of them operates in the superelastic regime (NiTi-1 Ni content of 50.5 at. %), while the other (NiTi-2 Ni content 50.1 at.%) exhibits shape memory behavior at room temperature.

The composition of the binder was adjusted from the multi-component binder system developed in a previous work [51]. The binder consists of the following components: stearic acid surfactant (SA, Sigma- Aldrich, USA), soluble thermoplastic elastomer (TPE, Kraiburg AG, German), partially soluble low-density polyethylene with a melt flow rate of 70 g/10 min (PE70, Arkema, France), and an insoluble low-density polyethylene with a melt flow rate of 2.63 g/10 min (PE3, Arkema, France). The exact feedstock composition can be found in Table 2. The constituent materials were compounded using a torque rheometer (HAAKE PolyLab OS, Thermo Fisher Scientific, USA) at 180 °C and 40 rpm for 30 min. Then the feedstocks were mechanically broken into small pieces and re-mixed for an additional 30 min at the same conditions. The feedstocks were prepared under Ar shield gas to minimize the oxidation of the powder. The oxidation of the powder in air was studied in a thermogravimetric analysis experiment. First signs of oxidation were observable from temperatures of ~ 185 °C (Supplementary Information, Fig. S2). Filaments were

**Table 1**

Composition of the two pre-alloyed powders, impurity levels and particle size distribution according to measurements performed by the supplier.

	Ti wt.%	Ni wt.%	C wt.%	O wt.%	N wt.%	H wt.%	D10 $\mu\text{m}$	D50 $\mu\text{m}$	D90 $\mu\text{m}$
NiTi-1	bal.	55.6	0.008	0.04	0.002	0.0008	7.04	14.77	24.67
NiTi-2	bal.	55.2	0.010	0.04	0.003	0.002	7.74	22.16	32.93

**Table 2**

Feedstock compositions used in this study. All values are in vol.%.

Alloy	LDPE3	LDPE70	TPE	SA	Powder
NiTi-1	12	15	18	5	50
NiTi-2	15	12	18	5	50

extruded using a capillary rheometer (RH7 Flowmaster, Netzsch, Germany) at 120 °C and a piston speed of 5 mm min<sup>-1</sup>, with a 1.8 mm die.

Specimens were 3D printed on a commercial FFF machine (Hephestos 2, BQ, Spain). The printing parameters can be found in Table 3. Residual stresses in the printed structures were relaxed by heating the parts to 120 °C and holding for 10 min in an oven (Function Line, Heraeus, Germany) in air atmosphere. The exact geometry of the specimens can be found in the Supplementary Information Fig. S3.

Solvent debinding of NiTi-2 specimens was performed in cyclohexane for 7 h at 60 °C using a magnetic stirrer with 10 rpm. During solvent debinding at 60 °C cracks were forming in the NiTi-1 specimens, similar to the ones observed previously in 316L steel feedstocks with low backbone contents of 7.5 vol% [51]. To prevent the formation of these defects, the solvent debinding step of the NiTi-1 feedstock was split into two stages. First, the TPE and stearic acid components were selectively removed in cyclohexane at 40 °C, and in a second step, the PE70 component was removed in cyclohexane at 60 °C. A short discussion of the two-stage solvent debinding procedure and the effective backbone content of the different feedstocks can be found in the Supplementary Information. After solvent debinding, the specimens were dried in air for 24 h and the weight loss was monitored. The average effective backbone content, consisting of the insoluble PE3 and the partially soluble PE70 is 21 vol% for both feedstocks.

Thermal debinding and sintering were performed in a retort furnace (VHT 08/16-Mo, Nabertherm GmbH, Germany) in Ar atmosphere (99.999 % purity, 100 L h<sup>-1</sup>). The following temperature profile was applied: heating from room temperature to 340 °C at 2 K min<sup>-1</sup>, heating to 470 °C at 0.5 K min<sup>-1</sup>, holding for 4 h, heating to 1290 °C at 5 K min<sup>-1</sup>, holding for 3 h.

## 2.2. Materials characterization

### 2.2.1. Scanning electron microscopy

For metallurgical examination of the sintered NiTi, cross-sections were prepared by Bakelite embedding (LaborPress-3, Struers GmbH, Switzerland), followed by grinding and polishing (RotPol-21, Struers GmbH, Switzerland; SiC 300, 600, 1200, 2400, 4000; diamond suspension 3  $\mu\text{m}$ , 1  $\mu\text{m}$ , 0.25  $\mu\text{m}$ ; Al<sub>2</sub>O<sub>3</sub> suspension 50 nm). Scanning electron microscopy (SEM) (JSM-7100F, JEOL Ltd., Japan) examination and energy dispersive X-ray (EDX) analysis (Ametek-EDAX detector) was performed to study the microstruc-

**Table 3**

Process parameters used for fused filament fabrication of the green body specimens.

D nozzle	T nozzle	T bed	Print speed	Layer height
0.4 mm	210 °C	60 °C	240 mm min <sup>-1</sup>	0.2 mm

tures after sintering. The porosity was measured optically by thresholding of the micrographs using ImageJ.

### 2.2.2. Differential scanning calorimetry

Differential scanning calorimetry (DSC) measurements (DSC 2500, TA Instruments, USA) of the two powders and the sintered material were performed between -90 °C and 160 °C at a rate of 10 K min<sup>-1</sup> in N<sub>2</sub> atmosphere. DSC specimens were cut from strained (4 %) sections of tensile samples to obtain conditions identical to the ones during the thermo-mechanical testing.

### 2.2.3. X-ray diffraction

The different NiTi phases present in both the powder and the sintered samples were studied by X-ray diffraction (XRD) (X'Pert MRD, Panalytical, Netherlands) equipped with a 0.27° parallel plate collimator, using a  $\Theta$ -2 $\Theta$  Bragg-Brentano configuration. Cu K $\alpha$ 1 ( $\lambda = 1.540598 \text{ \AA}$ ) radiation generated at 40 kV/45 mA was used. The final beam diameter was  $\sim 0.5 \text{ mm}$ . The angle range was selected to be 25 - 95 ([52]) 2 $\Theta$ , with a step size of 0.008° and 80 s per step. HighScore Plus software from Panalytical was used to remove the background and to qualitatively identify the phases.

### 2.2.4. Thermo-mechanical testing

The shape memory properties and ultimate tensile strength of the as-sintered NiTi were characterized on a universal testing machine (Instron E3000, Instron, USA) equipped with a climate chamber. The tensile specimens were tested with a 5 kN load cell and the actuator structures were tested with a 1 kN load cell. The specimens were strained at 0.067 % s<sup>-1</sup> to different levels and then unloaded to 1 N (tensile specimens), respectively 0.5 N (actuator specimens). The recovery strain was measured by applying a small constant force of 0.5 N, or 1 N respectively, while heating to 100 °C. The experimental strain calculated from the displacement of the testing machine actuator. The climate chamber used for heating prohibits the measurement of the strain by a mechanical extensometer or optical system. The strain of the actuator specimens was calculated as the effective strain given by the measured displacement divided by the initial length of the deforming components (excluding the clamping regions).

These measurements are affected by the thermal expansion of the testing set-up. This was compensated by subtracting the expansion measured during heating of the system without a specimen. However, the exact temperature distribution might deviate slightly between different experiments. This leads to an error in

the measured recovery strain, which is assumed to be in the order of 0.1 %.

The blocking force was measured by heating specimens after deformation, while keeping the displacement constant. The thermal expansion of the system cannot be compensated for in this experiment.

The plateau stress and plateau strain of the stress–strain curves was determined as the intersection of the initial linear elastic modulus with a line fitted to the plateau region. The total strain applied to the specimen consists of the following strain components: elastic strain  $\varepsilon_{el}$ , superelastic strain  $\varepsilon_{se}$ , shape memory strain  $\varepsilon_{sme}$ , and plastic strain  $\varepsilon_{pl}$ . After unloading at room temperature,  $\varepsilon_{el}$  and  $\varepsilon_{se}$  are recovered. The elastic portion of the recovered strain was calculated from the initial linear elastic modulus. The superelastic strain was obtained by subtracting the elastic component from the total recovered strain during unloading. The remnant strain after unloading is composed of a plastic component and the strain of detwinned martensite, which can be recovered. The latter was measured in a stress-free recovery experiment, such that the plastic strain could be determined.

### 2.3. Numerical simulations

The mechanical response of the different three geometries was studied by finite element analysis (Comsol Multiphysics 5.6). The structures were meshed with quadratic 3D tetrahedral elements with a constant size. The minimum number of elements across the narrowest region was 3. The mechanical response was modelled as linear elastic, with a Young's modulus of 29 GPa, obtained from experimental testing of NiTi-2, and a Poisson's ratio of 0.33 [53]. This assumption is valid for the small strains simulated (<0.5 %). The governing equations were solved using the multi-frontal direct sparse MUMPS solver.

In the simulations, the static side of the specimen was fixed, and a prescribed displacement was applied to the other end, such that a global effective strain of 0.4 % was reached. The effective strain of the actuators was calculated by dividing the applied deformation with the initial length of the deforming components (excluding the clamping region). The strain distribution of the different geometries was investigated in probability histograms, where the Y-axis shows the normalized number of elements, and the X-axis shows the normalized strain in the elements. Elements which belong to clamping regions were excluded from the analysis, as they do not experience strain when the structure is deformed. This representation is only valid if the element size is uniform throughout the geometry. If a locally refined mesh is used, the strain distribution in the histogram will be artificially skewed towards the strain of the refined regions.

## 3. Results

### 3.1. Microstructure of 3D-printed NiTi

The microstructure of the 3D-printed and sintered NiTi is examined by SEM. Fig. 1 shows polished cross-sections of the two alloys (left column NiTi-1, right column NiTi-2). During printing, the lower edge of the specimens was facing the print bed. The NiTi-1 specimen exhibits a porosity of 5 % and the porosity of the NiTi-2 specimens amounts to 12 %. The pores of the latter specimen appear more irregular and elongated. This is evidence for incomplete densification during sintering [54].

Two phases can be distinguished from the NiTi matrix by back scattered electron contrast. One phase is slightly darker, which can be identified as TiNi oxide by EDX (Fig. 1c, g). The other appears significantly darker and is found to be a Ti carbide with

elevated oxygen concentration. On the outside of the specimens a shell of brittle carbide and oxides is visible (Fig. 1c). In the low magnification image, the shell appears to be thinner on the NiTi-2 specimens. This is due to fracture of the brittle shell during specimen preparation, as it is indicated in Supplementary Information Fig. S5. The phases present in the powder and in the sintered specimens are studied by DSC and XRD. Fig. 2a, b shows the thermograms of the two powders and the sintered NiTi-1 (top) and NiTi-2 (bottom). The phase transitions in the two powders occur at very similar temperatures, despite the difference in Ni content. Multiple peaks can be observed for both transitions, martensite to austenite upon heating and the backward transition upon cooling. The start, peak, and finishing temperatures of the transitions as well as the heat of the phase transformation can be found in Table 4. The austenite transformation shifts to lower temperatures in the second heating cycle. This can potentially be attributed to changes in *meta*-stable phases in the powder.

After sintering, NiTi-1 (Fig. 2a) shows two very small peaks at  $-40$  °C and  $-17$  °C. The total heat of phase transformation of both peaks amounts to  $2.8 \text{ J g}^{-1}$ . No difference between the first and second heating cycle of the strained material is observed. The sintered NiTi-2 (Fig. 2b) shows an austenitic transformation upon heating and a backward transformation upon cooling. The endothermic peak of the second heating cycle is shifted to lower temperatures. The heat of phase transformation is lower compared to the one of the primary powders, as shown by the heat of the phase transformation (Table 4).

Fig. 2c, d shows the XRD patterns of the two NiTi alloys in the powder (blue) and the as-sintered state (magenta). The peaks of both NiTi powders coincide with B19' martensite pattern [52]. The NiTi-2 powder (Fig. 2d) exhibits two additional low-intensity peaks at  $35^\circ$  and  $40^\circ$ , which could be traces of elemental Ti. This phase might originate from the presence of elemental Ti during the atomization process. Sintered NiTi-1 (Fig. 2c) shows a predominant B2 austenitic pattern [55], while sintered NiTi-2 (Fig. 2d) exhibits both the B19' and B2 peaks, indicating that a mixture of austenite and martensite is present. The XRD patterns of both sintered NiTi alloys show low intensity peaks which are identified as TiNi-oxide and Ti-carbide. This is in agreement with the EDX results shown in Fig. 1, where the detected impurity phases (oxide and carbide) coincide with an enrichment in the Ti content. These impurities cannot be observed in the primary powders, indicating that they originate in the debinding and sintering process.

### 3.2. Thermo-mechanical properties of 3D-printed NiTi

Thermo-mechanical testing is performed to characterize the shape memory behavior of the two NiTi alloys. Fig. 3 shows the resulting stress–strain curves of tensile tests performed at room temperature (top row) and the stress-free recovery during heating (bottom row). Tensile specimens of the two alloys (Fig. 3 a, b) and actuator geometries of the NiTi-2 alloy (c, d) were tested.

The NiTi-2 specimen (Fig. 3 b) was loaded cyclically to measure the resulting strain components as a function of the applied strain. The remanent strain after unloading of the NiTi-2 specimen is much larger (2.5 %) than the residual strain of the NiTi-1 (Fig. 3 a) specimen (1.0 %), due to less elastic and superelastic strain recovery of the latter. After unloading of the NiTi-1 specimen, 1.3 % of strain were recovered due to superelasticity and 1.9 % were elastically recovered.

During heating across the austenite transformation temperature, the martensite is transformed to austenite and the shape memory strain,  $\varepsilon_{sme}$ , is recovered. Fig. 3e shows the heating of the NiTi-1 specimen. Only a very small decrease in strain with temperature can be observed, which is a small error introduced by the compensation of the thermal expansion of the test set-up. The

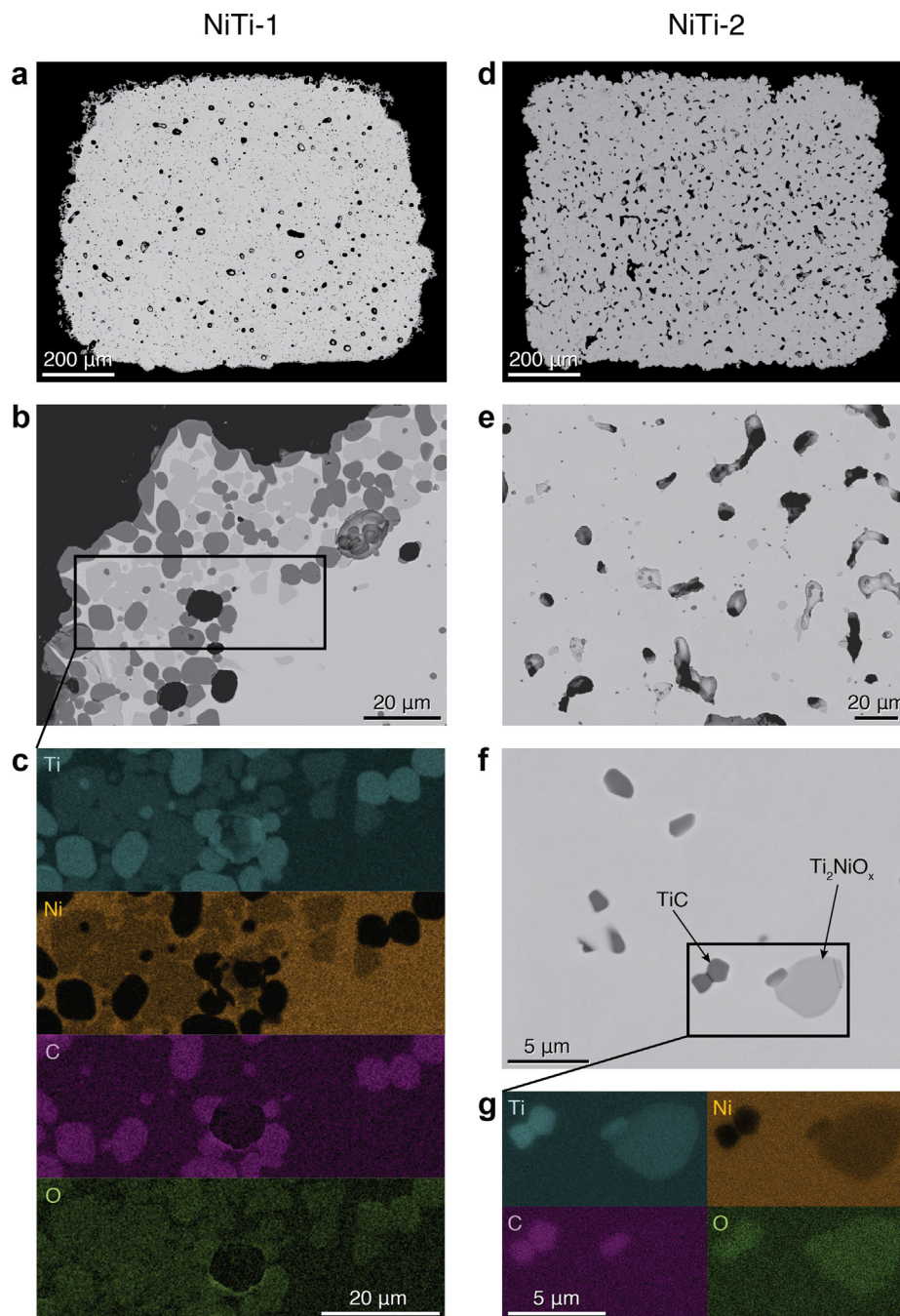


**Fig. 1.** SEM examination of polished cross-sections using the back scatter contrast. (a – c) NiTi-1, (d – g) NiTi-2. Two phases are visible, which appear darker than the NiTi matrix. EDX analysis indicates that the dark grey phase is a Ti carbide and the brighter is a TiNi oxide.

NiTi-2 specimen (Fig. 3 f) shows a strain recovery of 1.9 %. A small abrupt drop in stress can be observed in the stress–strain curves of both specimens, during straining in the plateau region. A possible explanation for this is localized crack formation in the surface, where SEM examination revealed a shell, embrittled by oxygen and carbon impurities. The plateau stress of the NiTi-1 alloy is much higher than the one of the NiTi-2 alloy. In Table 5 characteristic values of the stress–strain curves of both alloys are compared. The mechanical behavior of the actuator geometries will be discussed below.

Taking advantage of the design freedom of 3D printing, two types of actuators were fabricated from the NiTi-2 alloy, S-type actuators (see Fig. 3c), and  $\Omega$ -type actuators (d). The NiTi-2 alloy

was selected, such that the actuators exhibit a shape memory effect. The actuator geometries were designed with the objective to reduce the local strain in the material, preventing plastic deformation and thus, increasing the recoverable effective strain. The S-actuator shows a stress plateau similar to the one observed in the tensile specimen. The  $\Omega$ -type actuator does not exhibit a distinct plateau region even for large effective strains of 160 %. The portion of remnant strain after unloading, compared to the effective strain applied is much larger for the S-actuator (65 %) than for the  $\Omega$ -actuator (13 %), which recovers most of the applied strain elastically. The identification of the superelastic strain component using the initial linear-elastic modulus, performed for the S-actuator, might not be completely accurate, as the structure might not exhi-

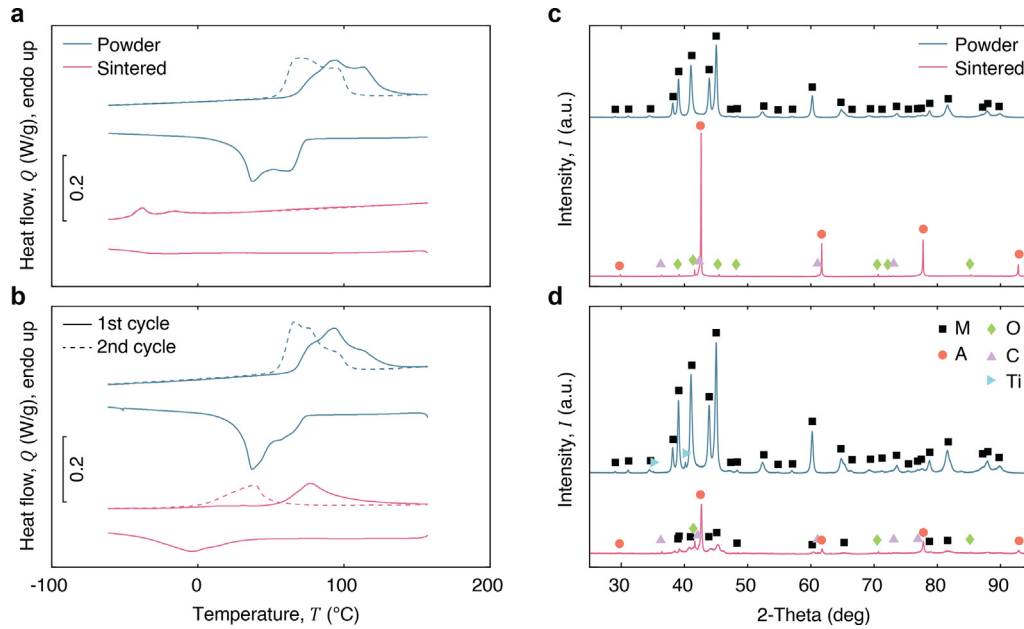


**Fig. 2.** DSC experiments and XRD patterns of the two alloys, as powder and sintered specimen. **Left: DSC.** The dashed line indicates the second heating cycle. In the powder state, NiTi-1 (a) and NiTi-2. (b) show similar temperatures for the martensite to austenite transformation upon heating and the backward transformation upon cooling. Both transformation peaks consist of multiple convoluted peaks. After sintering, NiTi-1 shows two small endothermic peaks on heating at temperatures of  $-40\text{ }^{\circ}\text{C}$  and  $-17\text{ }^{\circ}\text{C}$ . During cooling no peaks are visible. NiTi-2 exhibits a martensitic and a revers transformation peak. The latter shifts towards lower temperatures in the second heating cycle. **Right: XRD.** Legend in (d): M: NiTi B19' martensite (ICSD 164159), A: NiTi B2 austenite (ICSD 646945), O:  $\text{Ti}_4\text{Ni}_2\text{O}$  (ICSD 15809), C: TiC (ICSD 77168), Ti: elemental Ti  $\alpha'$  (ICSD 253841). NiTi-1 (c) and NiTi-2 (d) show almost identical martensitic patterns in the powder state. The pattern of sintered NiTi-1 mostly austenitic peaks, with some traces of carbide and oxide impurities. The peaks of sintered NiTi-2 can be identified as martensite, austenite, and small quantities of the carbide and oxide phase.

**Table 4**

Temperatures of phase transformations in sintered NiTi and in the primary powders for the first and the second cycle.

Alloy	$A_s$ $^{\circ}\text{C}$	$A_p$ $^{\circ}\text{C}$	$A_r$ $^{\circ}\text{C}$	$M_s$ $^{\circ}\text{C}$	$M_p$ $^{\circ}\text{C}$	$M_r$ $^{\circ}\text{C}$	Heat A $\text{Jg}^{-1}$	Heat M $\text{Jg}^{-1}$
NiTi-1 powder (1st)	65	94	132	73	37	20	27.4	26.8
NiTi-1 powder (2nd)	56	70	104				25.8	
NiTi-2 powder (1st)	66	93	135	73	37	23	27.4	26.4
NiTi-2 powder (2nd)	54	67	104				26.9	
NiTi-2 sintered (1st)	54	77	96	34	-4	-40	11.9	10.4
NiTi-2 sintered (2nd)	-2	39	57				12.5	

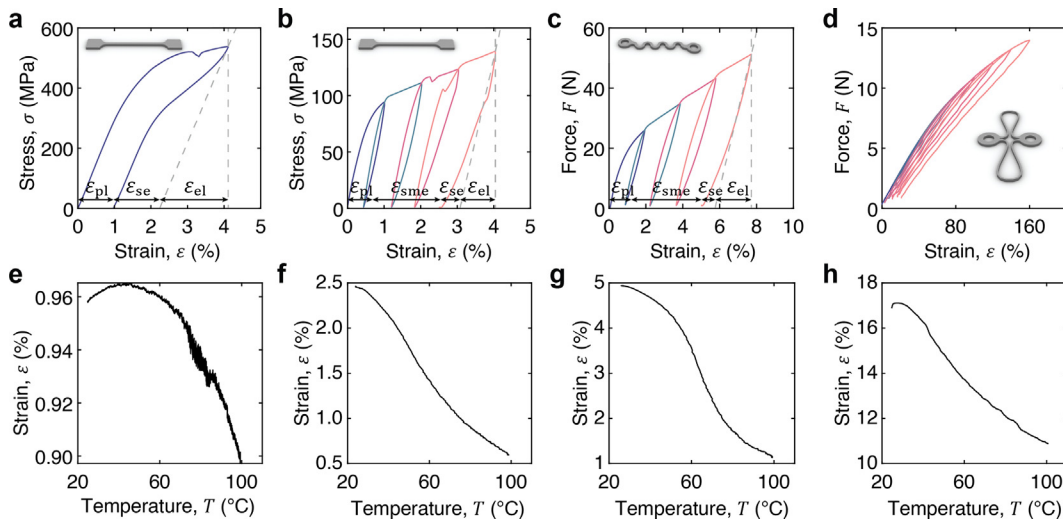


**Fig. 3.** Thermo-mechanical characterization of the 3D-printed SMAs. Elastic strain  $\epsilon_{el}$ , superelastic strain  $\epsilon_{se}$ , shape memory strain  $\epsilon_{sme}$ , and plastic strain  $\epsilon_{pl}$ . (a) Loading and unloading of a NiTi-1 tensile specimen, showing superelastic recovery. (b) Cyclic loading and unloading of a NiTi-2 tensile specimen. Cyclic loading and unloading of S-actuator (c) and  $\Omega$ -type actuator (d) 3D-printed from NiTi-2. (e-h) Stress-free recovery experiments. Upon heating the shape memory strain of the NiTi-2 specimens is recovered. The NiTi-1 sample does not show a shape memory effect. The small amount of recovered strain is due to an error introduced by the compensation of the thermal expansion.

**Table 5**

Stress–strain curve characteristics of the two alloys, and the NiTi-2 S-actuator. The values presented are the average of the specimens tested for thermo-mechanical characterization and the tensile tests until failure.

Specimen	Plateau stress (MPa)	Plateau strain (%)	Young's modulus (GPa)	UTS (MPa)	Elongation at break (%)
NiTi-1 tensile specimen	476	1.7	29	583	9.2
NiTi-2 tensile specimen	102 ± 12	0.5 ± 0.1	28 ± 3	505	17.7
NiTi-2 S-actuator	22	0.8			

bit a purely linear-elastic response. Yet, the shape of the force-strain curve allows for this analysis, and it can be utilized to compare the performance of the actuator to the bulk material. The reported values should however be interpreted with caution. Both actuator designs show significantly increased shape memory strains compared to the 3D-printed bulk NiTi-2 ( $\epsilon_{sme-S} = 3.8\%$ ,  $\epsilon_{sme-\Omega} = 6.2\%$ ). The strain components resulting from the cyclic loading–unloading experiments of NiTi-2 tensile specimen and the S-actuator, as well as the loading of a NiTi-1 tensile specimen are plotted in Fig. 4a, b.

Besides the actuation strain, the force generated is the second fundamental metric to evaluate the performance of actuators. This was tested for the different geometries of the NiTi-2 alloy in recovery experiments with constrained displacement. Fig. 5a–c shows the loading of a tensile specimen, an S-type actuator, and a  $\Omega$ -type actuator and d–f shows the respective actuation force, generated by the specimens upon heating. The maximum in the stress respectively force curves during heating occurs due to accelerated thermal expansion of the testing set-up at higher temperatures, as thermal expansion accelerates with increasing thermal gradients. The values reported here are most likely an underestimation due to this effect.

### 3.3. Numerical simulations of tested geometries

The numerical simulations performed show the distribution of the elastic strain in the different geometries. Fig. 6 depicts the distribution of the XX component of the elastic strain tensor. The displacement was applied in the x-direction such that an effective global strain of 4% was reached. As expected, the tensile specimen exhibits a homogeneous strain along the narrow region. Both actuator geometries show a larger variance in strain distribution, with most of the elements unstrained. The strain concentrates in the bend regions. Showing a bending load case with compression on the outside. The  $\Omega$ -actuator shows higher strain concentrations in the regions loaded in bending than the S-actuator. The histograms show a wider distribution of strain for the S-actuator than for the  $\Omega$ -actuator.

### 3.4. Mechanical properties of 3D-printed NiTi

Tensile tests were performed to examine the mechanical properties of the NiTi obtained from FFFm (Fig. 7a). Both alloys show an initial elastic regime with a modulus of  $\sim 29$  GPa. For larger strains the stress–strain curves differ significantly. The NiTi-1 specimen exhibits transition from the elastic region to the plateau at 467 MPa, followed by a plateau with nearly constant hardening until failure at a stress of 583 MPa and a strain of 9.2%. The NiTi-2 specimen shows the transition to the plateau at a lower stress of 110 MPa. An increase in hardening can be observed between 4% and 8% of strain, followed by the final section with a strain hardening similar to the one observed in the NiTi-1 specimen, until failure at a stress of 505 MPa and a strain of 17.7%. Values of the characteristic features of the stress–strain curves are summarized in Table 5. The fracture surface shows only limited signs of plastic deformation (Fig. 7b). Failure takes place by sudden catastrophic intergranular fracture without necking. The crack propagates along the grain boundaries. Precipitates, enriched in Ti, C, and O, and depleted in Ni, can be observed by high magnification SEM examination and EDX located along grain boundaries (Fig. 7c).

According to literature, the ultimate tensile strength of commercially fabricated NiTi is 754 – 960 MPa [56].

This is considerably higher than the tensile strength of our 3D-printed NiTi. Both the low mechanical properties compared to literature and the difference in strength between NiTi-1 and NiTi-2 can be attributed to porosity. In addition, intergranular precipitates, as they are found on the fracture surface, might lower the mechanical properties.

## 4. Discussion

### 4.1. Microstructure of 3D-printed NiTi

The SEM micrographs for both alloys show two types of precipitates dispersed in the NiTi matrix (Fig. 1).  $Ti_2NiO_x$  precipitates can be observed as medium-grey particles. The  $TiNi_2$  phase has a higher oxygen solubility than the NiTi matrix and interstitial oxygen atoms are reported to stabilize this phase [57,58]. This is confirmed by EDX showing Ti and O enrichment and Ni depletion

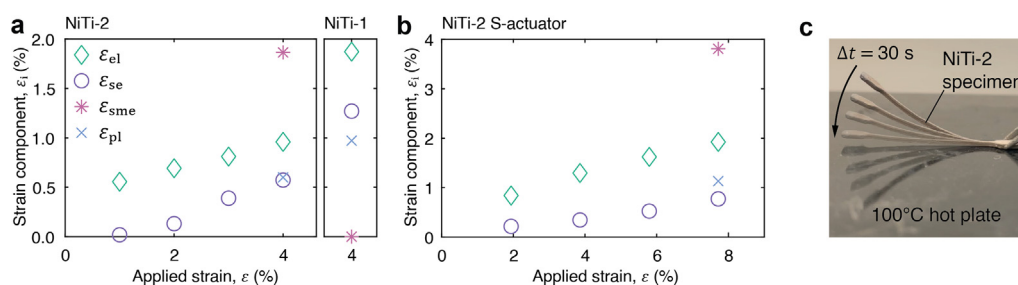


**Fig. 4.** Strain components during unloading and strain recovery of a NiTi-1 and a NiTi-2 tensile specimen (a) and a NiTi-2 S-actuator (b). Elastically recovered strain  $\epsilon_{el}$ , superelastically recovered strain  $\epsilon_{se}$ , shape memory strain  $\epsilon_{sme}$ , residual plastic deformation  $\epsilon_{pl}$ . (c) Overlay image of the qualitative shape recovery of a NiTi-2 tensile specimen on a hot plate at 100 °C. The specimen was bent manually. Upon heating the initial flat shape is recovered.



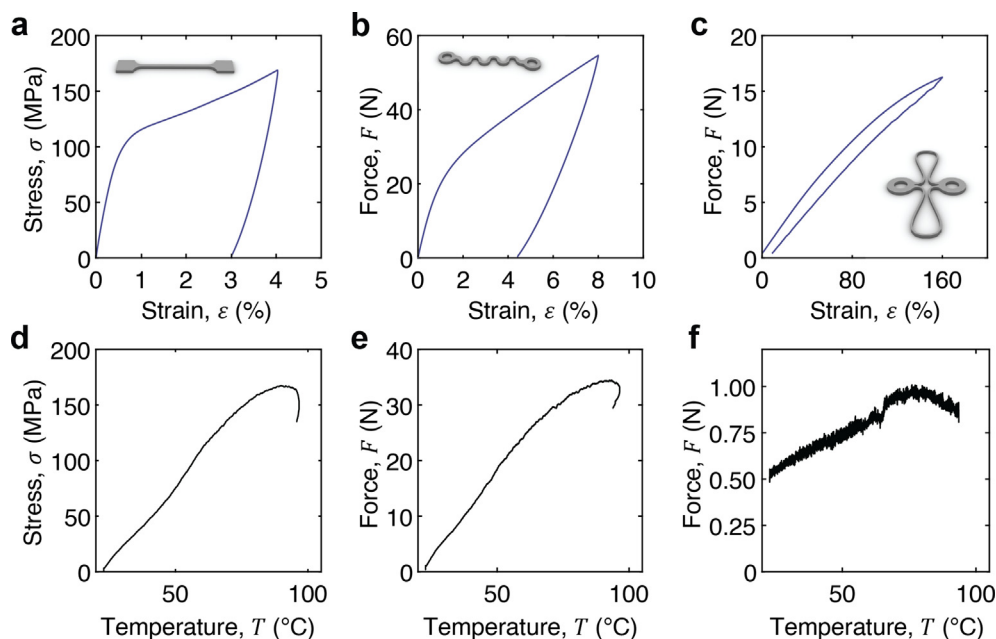


**Fig. 5.** Blocking stress respectively force by straining measured in constrained recovery experiment. Stress-strain curves (top row) and constrained recovery (bottom row) of a NiTi-2 tensile specimen (a, d), S-actuator (b, e), and  $\Omega$ -actuator (c, f). The tensile and spring geometry generate an actuation stress/force similar to the one applied during initial deformation. The  $\Omega$ -actuator produces only a very small actuation force.

relative to the NiTi matrix. The second particulate phase has darker color in the micrographs and is identified as TiC phase with an elevated content of O compared to the matrix. These impurities are commonly observed in sintered NiTi [49,53,59–62], resulting in a reduction of the Ti concentration in the matrix, and consequently in a lower phase transition temperature [57,63–65].

At the edge of the specimens, a shell region can be observed with a high density of oxide and carbide impurities. The thickness varies greatly between the edges facing the substrate and the atmosphere during sintering (from  $\sim 8 \mu\text{m}$  to  $\sim 39 \mu\text{m}$ ) (Supplementary Information Fig. S5). Further, the highest shell thickness can be observed on the top corners of the sample, which is the region where the specimens are exposed the most to the gas flow during sintering. This indicates that the shell is formed by reaction with the atmosphere, rather than exiting gaseous species from thermal debinding.

Interestingly, the sintered NiTi-1 appears to have lower porosity (5 %) than the NiTi-2 (12 %). Possible explanations for this observation could be an inhomogeneous temperature distribution in the sintering furnace (all specimens were sintered in a single batch), or a difference in the sintering kinetics between the two powders. The latter, however, seems unlikely, as the alloys are very similar in chemical composition, particle size distribution and morphology, and impurity contamination [54,66,67]. The D90 of the NiTi-2 powder is only about 33 % larger than the one of NiTi-1.

The effect of the stoichiometry of NiTi SMAs on the phase transition temperatures has been extensively studied [57,68]. Based on literature, the expected phase transition temperatures for our nominal Ni contents are:  $A_s(50.5 \text{ at.}\%) = 37 \text{ }^\circ\text{C}$  for NiTi-1, and  $A_s(50.1 \text{ at.}\%) = 72 \text{ }^\circ\text{C}$  for NiTi-2 [57]. As discussed above, impurities like carbon and oxygen can shift the effective Ni concentration in the matrix, resulting in lower phase transformation temperatures [57,63,64].

Despite this difference in chemical composition of the two alloys, the phase transformations in the powders, observed by DSC, happen almost at identical temperatures in both powders (Fig. 2a, b). This is surprising, considering the difference in Ni concentration, but might be due to heterogeneity in the local chemical

composition. As the powder is subjected to rapid quenching during the atomization process [69], local variations in Ni concentration appear plausible. The same reasoning can be used to explain the multiple convoluted peaks, which are visible over a very broad temperature range in the exothermic martensitic transformation and the reverse austenitic transformation (Fig. 2a, b). Multi-step transformations in NiTi have been ascribed to heterogeneity in the microstructure, i.e. changes in local Ni concentration due to precipitation of phases with off-stoichiometric Ni – Ti ratio, like  $\text{Ni}_4\text{Ti}_3$  [70]. The DSC results are in good agreement with the XRD examinations, showing a martensitic B19' pattern for both powders (Fig. 2c, d). The DSC curve of the sintered NiTi-1 alloy shows two small endothermic peaks ( $-40 \text{ }^\circ\text{C}$  and  $-17 \text{ }^\circ\text{C}$ ) during heating and no peaks during cooling. Such two-step transformations in NiTi were ascribed to the presence of the R-phase, which is an intermediate phase between martensite and austenite [71,72]. The low temperature peak represents the reaction of martensite to R and the smaller second peak is the reaction of R to austenite. No difference between the first and second heating cycle is visible. This observation is surprising, as no reverse transformation during cooling is visible. XRD performed at room temperature shows patterns of a prevalent austenite phase with TiC and oxygen stabilized  $\text{Ti}_2\text{NiO}_x$  (Fig. 2c). Both DSC and XRD analysis indicate a change in the phases between the powder and the sintered state. This shift from a martensite to an austenite phase can be ascribed to the uptake of Ti-rich impurities (carbide and oxide phases present in the XRD patterns and shown in the SEM micrographs (Fig. 1)).

The DSC curves of NiTi-2 in both states show an exothermic martensite peak and an endothermic peak for the reverse transformation during heating. The phase transformation temperatures after sintering are lower than in the primary powder and the peaks appear to be broadened, but as a single peak. This indicates that homogenization of the composition takes place during sintering at  $1290 \text{ }^\circ\text{C}$ . The decrease in the heat of phase transformation indicates a reduction in the martensitic NiTi phase fraction. This is consistent with the TiC,  $\text{Ti}_2\text{NiO}_x$ , and the austenite phase observed. The austenite peak in the strained NiTi-2 occurs at a higher temperature in the first heating cycle than in the second one (Table 4). It

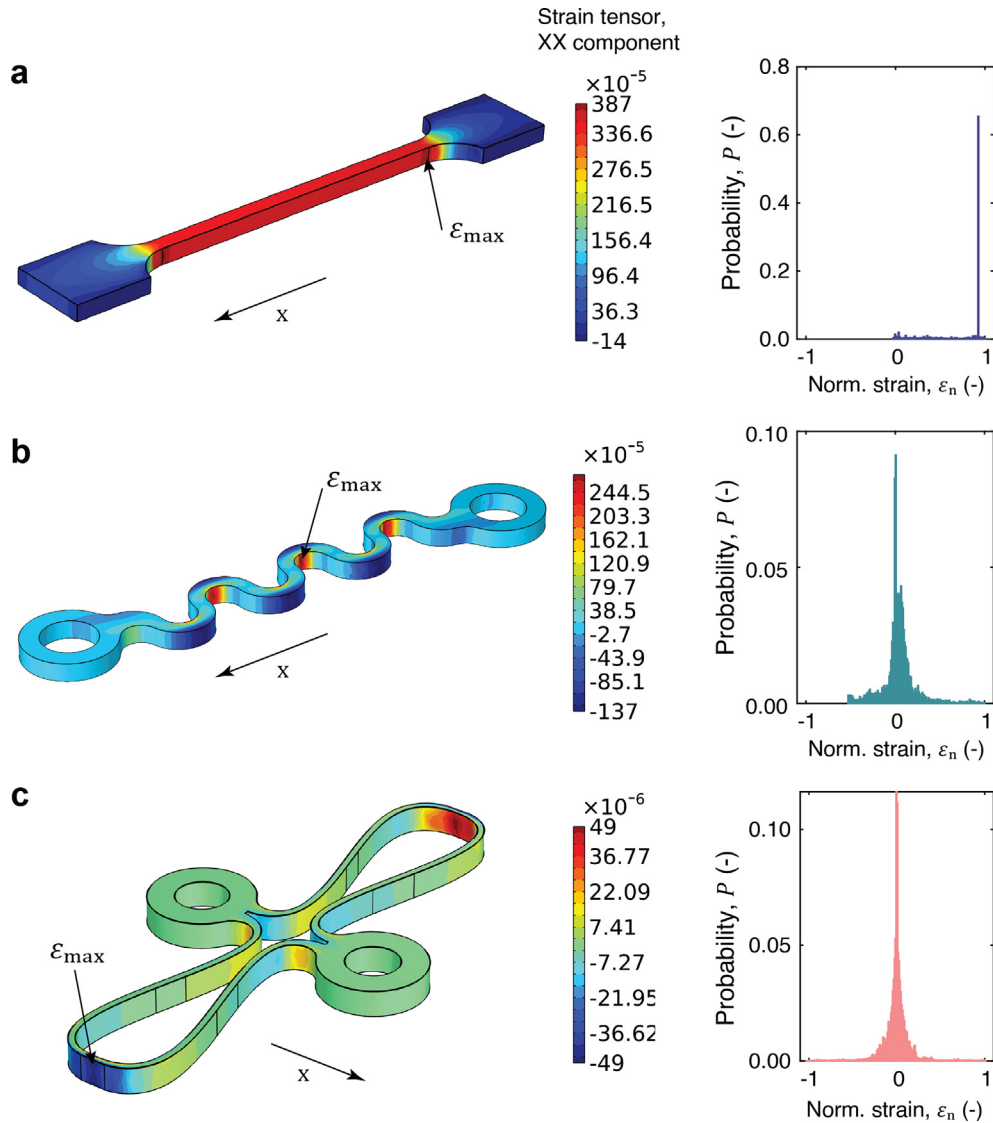


**Fig. 6. Numerical simulation of elastic strain and corresponding strain histograms, indicating the normalized XX component of the strain tensor.** A displacement is applied to all geometries, such that a nominal effective global strain of 0.4 % is obtained. (a) The tensile specimen shows a homogeneous strain distribution along the narrow region. (b) The S-actuator is loaded in bending with tensile and compressive loading on the outside respectively inside of the bends. (c) The  $\Omega$ -actuator again shows a bending, the strains are distributed less homogeneously than in the S-actuator.

is well known that the phase transformation temperatures in NiTi depend on the thermo-mechanical history of the specimen [73]. Shifts in the transformation temperatures of NiTi have been reported previously as a function of pre-strain with a plastic component. Dislocations induced by the deformation hinder the movement of interfaces and hence, increase the undercooling and overheating required for the phase transformation [74]. A similar line of argument can be used to develop a hypothesis for the lower austenite transformation temperature during the second heating. In the first cycle, the martensite is detwinned to favorable variants in the strained sample, with dislocations stabilizing the current martensite configuration. The austenite phase transformation of self-accommodated martensite, which is present in the second heating cycle, might require less overheating. The XRD patterns of the sintered NiTi-2 alloy show both peaks of the martensite phase and the austenite phase (Fig. 2d). The shift towards an austenitic phase at room temperature in the sintered samples compared to the martensitic primary powders in the NiTi-2 can be again attributed to the uptake of impurities. Unlike the NiTi-1 alloy, NiTi-2 retains some of its martensite phase at room temper-

ature after sintering. This can be explained by the higher Ti-content and therefore higher phase transformation temperatures of the NiTi-2 alloy.

#### 4.2. Thermo-mechanical properties of 3D-printed NiTi

The thermo-mechanical properties of the two alloys are consistent with the respective microstructures observed. NiTi-1, the alloy with high Ni content, shows an austenite phase at room temperature and hence exhibits superelasticity (Fig. 3a). After straining to about 4 %, a large portion of the strain is recovered elastically (1.9 %) and by the reverse transformation of the stress-induced martensite (1.3 %). The sintered NiTi-2 exhibits a mixture of the austenite and the martensite phase at room temperature. Hence, both superelastic ( $\epsilon_{se} = 0.6$  %) and shape memory behavior ( $\epsilon_{sme} = 1.9$  %) can be observed in the thermo-mechanical testing (Fig. 3b, f). Comparison of the strain components of the two alloys (Fig. 4a) shows that the plastic strain in the NiTi-1 is larger than in NiTi-2. This can be potentially attributed to the larger critical stress, required for the transformation of the austenite parent

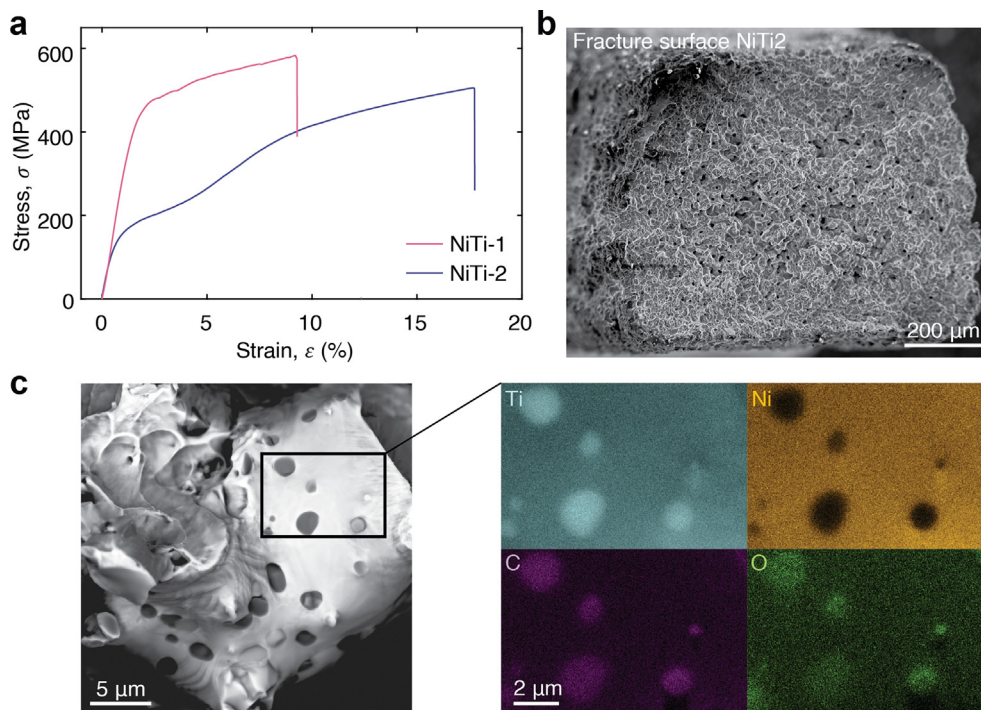


**Fig. 7. Tensile tests of the two 3D-printed NiTi alloys.** (a) Stress–strain curves of a NiTi-1 (magenta) and a NiTi-2 (blue) specimen, showing a large difference in plateau stress. (b) The fracture surface of the NiTi-2 specimen exhibits intergranular failure. (c) High magnification back scattered electron micrograph showing carbide precipitates located on the grain boundaries, as indicated by the elemental maps shown on the right. (For interpretation of the references to color in this figure legend, the reader is referred to the web version of this article.)

phase into martensite in NiTi-1, compared to the critical stress for detwinning of the martensite variants and formation of stress induced martensite in NiTi-2. The stress required can be described as the plateau stress of the stress–strain curves (Table 5). It is known to increase with temperature, as the stability of the austenitic phase increases [75,76]. This can be described by the Clausius – Clapeyron relation. The austenite transformation happens at much lower temperatures in the NiTi-1 (Fig. 2a), which is in accordance with the difference in stress–strain response observed. In general, low critical stresses for induction of superelastic and shape memory behavior are desirable. Like this, slip can be avoided, which would result in incomplete recovery of the shape, memorized by the austenite [75]. The recoverable strain measured in this work is lower than values reported in literature. Conventionally fabricated NiTi can exhibit shape memory strains up to 8 % [68]. For materials fabricated by SLM, recoverable strains up to 4.2 % have been reported [77]. In wire-based AM specimen up to 4.8 % of superelastic strain were observed. Various factors may contribute to the reduction in shape memory and superelastic strain in additively manufactured NiTi. The microstructure might contain phases which do not contribute to the shape memory effect, like  $Ti_2NiO_x$ , TiC,  $Ni_4Ti_3$  [29],  $Ni_3Ti$  [53], or phases which exhibit only a small shape memory effect like the R-phase [78]. The relatively small shape memory effect reported in this work might be due to severe uptake of oxygen and carbon during sintering at the high temperature of 1290 °C. Typically, lower sintering temperatures are used [60,62,79].

#### 4.3. FFFm of NiTi actuators

The actuators were designed with the objective to reduce the local strain in the material, such that large global deformations can be applied without inducing slip. The NiTi-2 material is selected for the actuators, such that they exhibit a shape memory

effect. Both the S-actuator as well as the  $\Omega$ -actuator geometry enable a reduction of the local strain in the material, as straining to 8 % respectively 160 % emphasizes (Fig. 3c, d). The S-actuator exhibits a plateau after initial elastic deformation similar to what is observed for the tensile specimens (Fig. 3b). In contrast to that, the stress–strain curve of the  $\Omega$ -actuator does not show a plateau. In the thermo-mechanical tests, all samples were strained to an effective strain of 4 %. After unloading during heating the tensile specimen recovers 47 % and the S-actuator recovers 49 % of the applied strain, while for the  $\Omega$ -actuator it is only 4 %. To investigate the origin of this remarkable discrepancy, the local strain distribution needs to be examined. This is facilitated by numerical simulations. Fig. 6 shows the three simulated geometries. The colors indicate the XX component of the elastic strain. As expected, the tensile specimen is uniformly strained in the narrow section, and the majority of all elements exhibit a strain close to the maximum strain. The S-actuator shows bending deformation with maximum positive respectively negative strain on the outside of the meanders.

The strain distribution in the  $\Omega$ -actuator again shows a bending deformation mode, on the very outside of the curves. The geometry dramatically lowers the strain in the material by almost one order of magnitude compared to the strain applied. However, the drawback of the actuator design is also clearly visible. The maximum strain is concentrated to an extremely small fraction of the material, while most of the material remains almost completely unstrained. With this finding in mind, we can explain the absence of a stress plateau mentioned before. Only a small amount of the material is loaded in the required strain window, in which martensite detwinning is induced and plastic deformation is avoided. Even for the high experimental strains of 160 %, large amount of the material is strained only elastically, the shape memory strain amounts to 6.2 %, and a plastic strain of 10.1 % remains after unloading and recovery. The same reasoning can be applied for

the interpretation of the blocking force measurements (Fig. 5). While the tensile specimen and the S-actuator are able to generate a stress respectively force similar to the one used for the initial deformation, almost no force is generated by the  $\Omega$ -actuator upon constraint heating.

This emphasizes a second design criterion for SMA actuators. Besides reducing the maximum local strain in the material, good actuator designs should have a strain distribution as uniform as possible when deformed. The  $\Omega$ -actuator used in this study is not a good actuator design. The geometry should be adjusted, such that the strain is distributed more uniformly. The S-actuator on the other hand, proved to successfully increase the actuation strain due to the shape memory effect by a factor of 2, while lowering the output force (the cross section of the tensile specimen is approximately 1 mm<sup>2</sup>) by a factor of 4.9.

## 5. Conclusions

This work demonstrates that filament-based 3D printing can be used to fabricate functional SMAs. The microstructural examination provides two implications for the binder design of NiTi filaments. First, the introduction of carbon impurities in the material and hence the backbone content removed by pyrolysis needs to be minimized while preventing defect formation during debinding. The use of a two-stage solvent debinding step, as discussed in the [Supplementary Information](#), appears recommendable to prevent crack formation. In addition, it is advantageous to select a backbone polymer with a low thermal decomposition temperature and low carbon residue. Second, the purity of the sintering atmosphere is of greatest importance, due to the high reactivity of the Ti. The sintering process used in this work can be improved by selecting a lower sintering temperature and using an oxygen getter for purification of the atmosphere.

Both superelastic and shape memory properties are obtained for the two 3D-printed alloys. The characterized microstructures are consistent with the results of the thermo-mechanical tests. After straining to 4 %, NiTi-1 shows 1.2 % superelastic strain recovery, while NiTi-2 shows a shape memory strain of 1.9 %. The values obtained here are lower than literature reports and can be potentially improved by optimization of the binder composition and the sintering conditions, as discussed above.

Two types of actuators were fabricated from the NiTi-2 alloy. The S-actuator shows an improved actuation displacement compared to the bulk material. Numerical simulation of the different structures allows to explain the observed actuator performances and emphasizes the importance of a uniform distribution of strain for good actuator designs. The findings reported in this work, could find immediate applications in 3D-printed active devices utilizing the superelastic and the and shape memory properties of NiTi, e.g. by combination of both of the alloys into one structure. The utilization of metallic materials has the potential to increase the capabilities of the structures fabricated by 4D printing and overcome current limitations associated with polymeric materials.

## Data availability

Data will be made available on request.

## Declaration of Competing Interest

The authors declare that they have no known competing financial interests or personal relationships that could have appeared to influence the work reported in this paper.

## Acknowledgement

The authors would like to acknowledge the numerous contributions to this work. Dr. Fabio Krogh and Beatrice Wegmann contributed by building experimental set-ups. Dr. Mikel Rodriguez-Arbaizar and Prof. Dr. Efrain Carreño-Morelli have supported this work by helping to perform the sintering experiments. The authors also acknowledge support of the Scientific Center for Optical and Electron Microscopy (ScopeM). This study is part of the strategic focus area advanced manufacturing project "Sustainable Design of 4D Printed Active Systems (SD4D)" of the ETH domain, Switzerland.

## Data availability

Data supporting the findings of this study are available from the corresponding authors on request.

## Appendix A. Supplementary data

Supplementary data to this article can be found online at <https://doi.org/10.1016/j.matdes.2022.111418>.

## References

- [1] F. Demoly, M.L. Dunn, K.L. Wood, H.J. Qi, J.-C. André, The status, barriers, challenges, and future in design for 4d printing, *Mater. & Des.*, vol. 212, p. 110 193, 2021.
- [2] D.C. Lagoudas, *Shape memory alloys: modeling and engineering applications*, Springer (2008) 19–20.
- [3] A. Nespoli, S. Besseghini, S. Pittaccio, E. Villa, S. Viscuso, The high potential of shape memory alloys in developing miniature mechanical devices: A review on shape memory alloy mini-actuators, *Sens. Actuators, A* 158 (1) (2010) 149–160.
- [4] M.H. Elahinia, *Shape memory alloy actuators: design, fabrication, and experimental evaluation*, John Wiley & Sons 92 (2016), et sqq.
- [5] W. Huang, On the selection of shape memory alloys for actuators, *Mater. Des.* 23 (1) (2002) 11–19.
- [6] N. Sabahi, W. Chen, C.-H. Wang, J.J. Kruzic, X. Li, A review on additive manufacturing of shape-memory materials for biomedical applications, *JOM* 72 (3) (2020) 1229–1253.
- [7] J.M. Jani, M. Leary, A. Subic, M.A. Gibson, A review of shape memory alloy research, applications and opportunities, *Mater. Des.* 1980–2015 (56) (2014) 1078–1113.
- [8] M. Zhang et al., 3d printed mg-niti interpenetrating-phase composites with high strength, damping capacity, and energy absorption efficiency, *Sci. Adv.* vol. 6, no. 19 (2020) eaba5581.
- [9] C. Haberland, M. Elahinia, J.M. Walker, H. Meier, J. Frenzel, On the development of high quality niti shape memory and pseudoelastic parts by additive manufacturing, *Smart Mater. Struct.*, vol. 23, no. 10, p. 104 002, 2014.
- [10] T. Yao, Y. Wang, B. Zhu, D. Wei, Y. Yang, X. Han, 4d printing and collaborative design of highly flexible shape memory alloy structures: A case study for a metallic robot prototype, *Smart Mater. Struct.*, vol. 30, no. 1, p. 015 018, 2020.
- [11] M. Speirs, B. Van Hooreweder, J. Van Humbeeck, J.-P. Kruth, Fatigue behaviour of niti shape memory alloy scaffolds produced by slm, a unit cell design comparison, *J. Mech. Behav. Biomed. Mater.* 70 (2017) 53–59.
- [12] C. Haberland, H. Meier, J. Frenzel, On the properties of ni-rich niti shape memory parts produced by selective laser melting, *Smart Materials Adaptive Structures and Intelligent Systems*, American Society of Mechanical Engineers 45097 (2012) 97–104.
- [13] X. Yang, et al., Effect of volume fraction and unit cell size on manufacturability and compressive behaviors of ni-ti triply periodic minimal surface lattices, *Additive Manuf.*, vol. 54, p. 102 737, 2022.
- [14] M. Zhao, et al., Superelastic behaviors of additively manufactured porous niti shape memory alloys designed with menger sponge-like fractal structures, *Mater. & Des.*, vol. 200, p. 109 448, 2021.
- [15] M.H. Wu, Fabrication of nitinol materials and components, *Materials Science Forum Trans Tech Publ* 394 (2002) 285–292.
- [16] S. Wu, H. Lin, C. Chen, A study on the machinability of a ti49. 6ni50. 4 shape memory alloy, *Mater. Lett.* 40 (1) (1999) 27–32.
- [17] T. Gustmann et al., Properties of a superelastic niti shape memory alloy using laser powder bed fusion and adaptive scanning strategies, *Prog. Additive Manuf.* 5 (1) (2020) 11–18.
- [18] M. Elahinia et al., Additive manufacturing of niti high temperature shape memory alloy, *Scr. Mater.* 145 (2018) 90–94.
- [19] H. Lu, et al., Ultrahigh-performance tini shape memory alloy by 4d printing, *Mater. Sci. Eng.: A*, vol. 763, p. 138 166, 2019.

- [20] J. Ma et al., Spatial control of functional response in 4d-printed active metallic structures, *Sci. Rep.* 7 (1) (2017) 1–8.
- [21] C. Lauthoff et al., Additive manufacturing of co-ni-ga high-temperature shape memory alloy: Process-ability and phase transformation behavior, *Metall. Mater. Trans. A* 51 (3) (2020) 1056–1061.
- [22] A. Agrawal, R.K. Dube, Methods of fabricating cu-al-ni shape memory alloys, *J. Alloy. Compd.* 750 (2018) 235–247.
- [23] G. Dennis, J. Santos, C.S. Kiminami, P. Gargarella, Comparison of cu-al-ni-mn-zr shape memory alloy prepared by selective laser melting and conventional powder metallurgy, *Trans. Nonferrous Met. Soc. Chin.* 30 (12) (2020) 3322–3332.
- [24] I. Ferretto, D. Kim, N. Della Ventura, M. Shahverdi, W. Lee, C. Leinenbach, Laser powder bed fusion of a fe-mn-si shape memory alloy, *Additive Manuf.*, vol. 46, p. 102 071, 2021.
- [25] L. Patriarca, W. Abuzaid, G. Carlucci, F. Bellelli, R. Casati, Pseudoelasticity in femoral shape memory alloy lattice structures produced by laser powder bed fusion, *Mater. Lett.*, vol. 302, p. 130 349, 2021.
- [26] V. Laitinen, A. Sozinov, A. Saren, A. Salminen, K. Ullakko, Laser powder bed fusion of ni-mn-ga magnetic shape memory alloy, *Additive Manuf.*, vol. 30, p. 100 891, 2019.
- [27] I.F. Ituarte, F. Nilsén, V.K. Nadimpalli, M. Salmi, J. Lehtonen, S.-P. Hannula, Towards the additive manufacturing of ni-mn-ga complex devices with magnetic field induced strain, *Additive Manuf.*, vol. 49, p. 102 485, 2022.
- [28] V. Laitinen, A. Saren, A. Sozinov, K. Ullakko, Giant 5.8% magnetic-field-induced strain in additive manufactured ni-mn-ga magnetic shape memory alloy, *Scripta Materialia*, vol. 208, p. 114 324, 2022.
- [29] D. Zhang, Y. Li, W. Cong, Multi-scale pseudoelasticity of niti alloys fabricated by laser additive manufacturing, *Mater. Sci. Eng.: A*, vol. 821, p. 141 600, 2021.
- [30] D. Gu, C. Ma, In-situ formation of ni<sub>4</sub>ti<sub>3</sub> precipitate and its effect on pseudoelasticity in selective laser melting additive manufactured niti-based composites, *Appl. Surf. Sci.* 441 (2018) 862–870.
- [31] G.R. Donoso, M. Walczak, E.R. Moore, J.A. Ramos-Grez, Towards direct metal laser fabrication of cu-based shape memory alloys, *Rapid Prototyp. J.* (2017).
- [32] C. Lauthoff et al., Excellent superelasticity in a co-ni-ga high-temperature shape memory alloy processed by directed energy deposition, *Mater. Res. Lett.* 8 (8) (2020) 314–320.
- [33] Z. Zeng, et al., Wire and arc additive manufacturing of a ni-rich niti shape memory alloy: Microstructure and mechanical properties, *Additive Manuf.*, vol. 32, p. 101 051, 2020.
- [34] N. Resnina, et al., Structure, martensitic transformations and mechanical behaviour of niti shape memory alloy produced by wire arc additive manufacturing, *J. Alloys Compd.*, vol. 851, p. 156 851, 2021.
- [35] M. Caputo, C. Solomon, A facile method for producing porous parts with complex geometries from ferromagnetic ni-mn-ga shape memory alloys, *Mater. Lett.* 200 (2017) 87–89.
- [36] M.P. Caputo, A.E. Berkowitz, A. Armstrong, P. Müllner, C.V. Solomon, 4d printing of net shape parts made from ni-mn-ga magnetic shape-memory alloys, *Addit. Manuf.* 21 (2018) 579–588.
- [37] A. Mostafaei et al., Microstructural evolution and magnetic properties of binder jet additive manufactured ni-mn-ga magnetic shape memory alloy foam, *Acta Mater.* 131 (2017) 482–490.
- [38] E. Carreño-Morelli, S. Martinerie, J.E. Bidaux, Three-dimensional printing of shape memory alloys, *Materials science forum*, *Trans Tech Publ* 534 (2007) 477–480.
- [39] S.L. Taylor, A.J. Ibeh, A.E. Jakus, R.N. Shah, D.C. Dunand, Niti-nb micro-trusses fabricated via extrusion-based 3d-printing of powders and transient-liquid-phase sintering, *Acta Biomater.* 76 (2018) 359–370.
- [40] R. Agrawal, F. Anantachaisilp, J. Tirano, H.Z. Ramirez, Z. Marquez, C. Luhrs, Paste-based 3d printing of metallic materials: Effect of binders and precursor sizes, *Mater. Res. Express*, vol. 6, no. 10, p. 106 561, 2019.
- [41] S.L. Taylor, R.N. Shah, D.C. Dunand, Ni-mn-ga micro-trusses via sintering of 3d-printed inks containing elemental powders, *Acta Mater.* 143 (2018) 20–29.
- [42] P. Carreira, F. Cerejo, N. Alves, M.T. Vieira, In search of the optimal conditions to process shape memory alloys (niti) using fused filament fabrication (fff), *Materials* 13 (21) (2020) 4718.
- [43] K. Otsuka, C.M. Wayman, *Shape memory materials*, Cambridge University Press, 1999, p. 242.
- [44] Z. Zhakypov, J.-L. Huang, J. Paik, A novel torsional shape memory alloy actuator: Modeling, characterization, and control, *IEEE Rob. Autom. Mag.* 23 (3) (2016) 65–74.
- [45] M.F. Ashby, The properties of foams and lattices, *Philos. Trans. Royal Soc. A: Math., Phys. Eng. Sci.* 364 (1838) (2006) 15–30.
- [46] A. Bansiddhi, D.C. Dunand, Shape-memory niti foams produced by solid-state replication with naf, *Intermetallics* 15 (12) (2007) 1612–1622.
- [47] A. Bansiddhi, D. Dunand, Shape-memory niti foams produced by replication of nacl space-holders, *Acta Biomater.* 4 (6) (2008) 1996–2007.
- [48] J. Xiong, Y. Li, X. Wang, P. Hodgson, C. Wen, Titanium-nickel shape memory alloy foams for bone tissue engineering, *J. Mech. Behav. Biomed. Mater.* 1 (3) (2008) 269–273.
- [49] M. Köhl, T. Habijan, M. Bram, H.P. Buchkremer, D. Stöver, M. Köller, Powder metallurgical near-net-shape fabrication of porous niti shape memory alloys for use as long-term implants by the combination of the metal injection molding process with the space-holder technique, *Adv. Eng. Mater.* 11 (12) (2009) 959–968.
- [50] C. Wen, J. Xiong, Y. Li, P. Hodgson, Porous shape memory alloy scaffolds for biomedical applications: A review, *Physica Scripta*, vol. 2010, no. T139, p. 014 070, 2010.
- [51] M.A. Wagner, et al., Fused filament fabrication of stainless steel structures-from binder development to sintered properties, *Additive Manuf.*, p. 102 472, 2021.
- [52] H. Sitepu, In situ structural and texture analyses of monoclinic phase for polycrystalline ni-rich ti<sub>49</sub>. 86ni<sub>50</sub>. 14 alloy from neutron diffraction data, *Powder Diffr.* 23 (1) (2008) 35–40.
- [53] Z. Wang, J. Chen, C. Besnard, L. Kunčická, R. Kocich, A.M. Korsunsky, In situ neutron diffraction investigation of texture-dependent shape memory effect in a near equiatomic niti alloy, *Acta Mater.* 202 (2021) 135–148.
- [54] R.M. German, *Sintering theory and practice*, 1996.
- [55] F. Van Loo, G. Bastin, A. Leenen, Phase relations in the ternary ti-ni-cu system at 800 and 870 °C, *J. Less Common Metals* 57 (1) (1978) 111–121.
- [56] *MatWeb Material Property Data, NiTi low temperature phase*, <https://www.matweb.com/search/DataSheet.aspx?MatGUID=44afc7d3c6eb4829bc2df27884fd2d6c>, Accessed: 2022-04-05.
- [57] J. Frenzel, E.P. George, A. Dlouhy, C. Somsen, M.-X. Wagner, G. Eggeler, Influence of ni on martensitic phase transformations in niti shape memory alloys, *Acta Mater.* 58 (9) (2010) 3444–3458.
- [58] R. Mackay, G.J. Miller, H.F. Franzen, New oxides of the filled-ti<sub>2</sub>ni type structure, *J. Alloy. Compd.* 204 (1–2) (1994) 109–118.
- [59] J. Mentz, M. Bram, H.P. Buchkremer, D. Stöver, Improvement of mechanical properties of powder metallurgical niti shape memory alloys, *Adv. Eng. Mater.* 8 (4) (2006) 247–252.
- [60] M.H. Ismail, R. Razali, Z. Abdullah, I. Subuki, N. Muhamad, Shape memory behaviour of niti alloy produced by mim using palm stearin based binder, *Advanced Materials Research*, *Trans Tech Publ* 1133 (2016) 295–299.
- [61] L. Krone et al., The potential of powder metallurgy for the fabrication of biomaterials on the basis of nickel-titanium: A case study with a staple showing shape memory behaviour, *Adv. Eng. Mater.* 7 (7) (2005) 613–619.
- [62] E. Schöller, L. Krone, M. Bram, H. Buchkremer, D. Stöver, Metal injection molding of shape memory alloys using prealloyed niti powders, *J. Mater. Sci.* 40 (16) (2005) 4231–4238.
- [63] J. Otubo, O. Rigo, C.M. Neto, P. Mei, The effects of vacuum induction melting and electron beam melting techniques on the purity of niti shape memory alloys, *Mater. Sci. Eng. A* 438 (2006) 679–682.
- [64] J. Frenzel, Z. Zhang, C. Somsen, K. Neuking, G. Eggeler, Influence of carbon on martensitic phase transformations in niti shape memory alloys, *Acta Mater.* 55 (4) (2007) 1331–1341.
- [65] K. Otsuka, C.M. Wayman, *Shape memory materials*, Cambridge University Press, 1999, p. 72.
- [66] P.M. Derlet, *Sintering theory*, Paul Scherrer Institut, 2017, p. 73.
- [67] R. German, *Sintering: from empirical observations to scientific principles*, Butterworth-Heinemann, 2014, p. 156.
- [68] D.C. Lagoudas, *Shape memory alloys: modeling and engineering applications*, Springer, 2008, p. 24.
- [69] R.M. German, *Supersolidus liquid-phase sintering of prealloyed powders*, *Metall. Mater. Trans. A* 28 (7) (1997) 1553–1567.
- [70] J. Khalil-Allafi, A. Dlouhy, G. Eggeler, Ni<sub>4</sub>ti<sub>3</sub>-precipitation during aging of niti shape memory alloys and its influence on martensitic phase transformations, *Acta Mater.* 50 (17) (2002) 4255–4274.
- [71] G. Eggeler, J. Khalil-Allafi, S. Gollerthan, C. Somsen, W. Schmahl, D. Sheptyakov, On the effect of aging on martensitic transformations in ni-rich niti shape memory alloys, *Smart Mater. Struct.* 14 (5) (2005) S186.
- [72] J. Kim, Y. Liu, S. Miyazaki, Ageing-induced two-stage r-phase transformation in ti–50.9 at.% ni, *Acta Mater.* 52 (2) (2004) 487–499.
- [73] D.C. Lagoudas, *Shape memory alloys: modeling and engineering applications*, Springer, 2008, pp. 82–83.
- [74] K. Fukami-Ushiro, D. Dunand, Niti and niti-tic composites: Part iii. shape-memory recovery, *Metall. Mater. Trans. A* 27 (1) (1996) 193–203.
- [75] K. Otsuka, C.M. Wayman, *Shape memory materials*, Cambridge University Press, 1999, p. 40.
- [76] Y. Liu, A. Mahmud, F. Kursawe, T.-H. Nam, Effect of pseudoelastic cycling on the clausius–clapeyron relation for stress-induced martensitic transformation in niti, *J. Alloys Compd.* 449 (1–2) (2008) 82–87.
- [77] S. Saedi, A.S. Turabi, M.T. Andani, C. Haberland, H. Karaca, M. Elahinia, The influence of heat treatment on the thermomechanical response of ni-rich niti alloys manufactured by selective laser melting, *J. Alloy. Compd.* 677 (2016) 204–210.
- [78] K. Otsuka, C.M. Wayman, *Shape memory materials*, Cambridge University Press (1999) 59–65.
- [79] S. Green, D. Grant, N. Kelly, Powder metallurgical processing of ni–ti shape memory alloy, *Powder Metall.* 40 (1) (1997) 43–47.